

## TWO-DIMENSIONAL NUMERICAL SIMULATIONS OF SUPERCRITICAL ACCRETION FLOWS REVISITED

XIAO-HONG YANG<sup>1,2</sup>, FENG YUAN<sup>1</sup>, KEN OHSUGA<sup>3</sup>, AND DE-FU BU<sup>1</sup>*Draft version June 7, 2018*

## ABSTRACT

We study the dynamics of super-Eddington accretion flows by performing two-dimensional radiation-hydrodynamic simulations. Compared with previous works, in this paper we include the  $T_{\theta\phi}$  component of the viscous stress and consider various values of the viscous parameter  $\alpha$ . We find that when  $T_{\theta\phi}$  is included, the rotational speed of the high-latitude flow decreases, while the density increases and decreases at the high and low latitudes, respectively. We calculate the radial profiles of inflow and outflow rates. We find that the inflow rate decreases inward, following a power law form of  $\dot{M}_{\text{in}} \propto r^{-s}$ . The value of  $s$  depends on the magnitude of  $\alpha$  and is within the range of  $\sim 0.4 - 1.0$ . Correspondingly, the radial profile of density becomes flatter compared with the case of a constant  $\dot{M}(r)$ . We find that the density profile can be described by  $\rho(r) \propto r^{-p}$  and the value of  $p$  is almost same for a wide range of  $\alpha$  ranging from  $\alpha = 0.1$  to  $0.005$ . The inward decrease of inflow accretion rate is very similar to hot accretion flows, which is attributed to the mass loss in outflows. To study the origin of outflow, we analyze the convective stability of the slim disk. We find that depending on the value of  $\alpha$ , the flow is marginally stable (when  $\alpha$  is small) or unstable (when  $\alpha$  is large). This is different from the case of hydrodynamical hot accretion flow where radiation is dynamically unimportant and the flow is always convectively unstable. We speculate that the reason for the difference is because radiation can stabilize convection. The origin of outflow is thus likely because of the joint function of convection and radiation, but further investigation is required.

*Subject headings:* accretion, accretion disk – black hole physics – hydrodynamics – methods: numerical – radiative transfer

## 1. INTRODUCTION

One milestone in black hole accretion is the standard thin disk model (Shakura & Sunyaev 1973; Pringle 1981). This model applies below the Eddington accretion rate defined as  $\dot{M}_{\text{Edd}} \equiv 10L_{\text{Edd}}/c^2$  ( $L_{\text{Edd}}$  is the Eddington luminosity). In this model, all the viscously dissipated energy is immediately radiated away. When the accretion rate is above the Eddington rate, advection begins to become important and the accretion model is described by the “slim disk” (Abramowicz et al. 1988; see also Begelman & Meier 1982). In a slim disk, the radiative efficiency is lower than that of the standard thin disk because of energy advection and photons trapping effects. The energy dissipated in the disk is advected with the accreting matter, since the radiative diffusion timescale is longer than the accretion timescale. Note that the slim-disk model cannot correctly treat the photon trapping, because photon trapping is basically a multi-dimensional effect (Ohsuga et al. 2002; 2003). The potential applications of slim-disks include narrow-line Seyfert galaxies (Mineshige et al. 2000) and ultraluminous X-ray sources (Watarai et al. 2001; Vierdayanti et al. 2006).

The above-mentioned pioneer works on slim disk are all one dimensional and analytical. Multi-dimensional and time-dependent numerical simulations obviously can reveal important additional information about the dynam-

ics of the accretion flow. Many radiation-hydrodynamic (RHD; Eggum et al. 1987, 1988; Okuda 2002; Okuda et al. 2005; Ohsuga et al. 2005) and radiation magnetohydrodynamic (MHD; Ohsuga et al. 2009; Ohsuga & Mineshige 2011) numerical simulation works on slim disk have been performed. Among these works, Ohsuga et al. (2005) obtain a quasi-steady structure of the supercritical accretion flows and outflows by a two-dimensional global simulation. Their results broadly confirm the main properties predicted by the analytical slim-disk model. Moreover, they show that the accretion flow is composed of the disk region around the equatorial plane and the outflow region above and below the disk. Ohsuga & Mineshige (2007) further identify that the supercritical accretion is feasible because a very large radiation energy density actually produces a small radiative flux as well as a force, because of the large optical depth and photon trapping effects.

Recently, there are some works studying the thermal stability of radiation pressure dominated thin disk using shearing box MHD numerical simulation with radiative transfer (Hirose et al. 2009; Jiang et al. 2013). Hirose et al. (2009) found that the disk is thermally stable, while Jiang et al. (2013) found that it is unstable. The reason for the discrepancy is discussed in the latter work.

In the RHD simulation of Ohsuga et al. (2005), an anomalous shear stress is included to mimic the angular momentum transfer. However, in reality, we expect Maxwell stresses associated with MHD turbulence driven by the magneto-rotational instability (MRI) to provide angular momentum transport in accretion flows (Balbus & Hawley 1998). Since MRI is driven only by shear associated with the orbital dynamics, when an anomalous

<sup>1</sup> Shanghai Astronomical Observatory, Chinese Academy of Sciences, 80 Nandan Road, Shanghai 200030, China; yangxh@cqu.edu.cn, fyuan@shao.ac.cn

<sup>2</sup> Department of Physics, Chongqing University, Chongqing 400044, China

<sup>3</sup> National Astronomical Observatory of Japan, Osawa, Mitaka, Tokyo 181-8588, Japan

shear stress is adopted we should only set the two azimuthal components ( $r\phi$  and  $\theta\phi$ ) of the stress tensor to be non-zero (Stone et al. 1999). This is confirmed by the local shearing box simulations, which indicate that the azimuthal components of the Maxwell stress are one order of magnitude larger than the poloidal components (e.g., Hawley et al. 1995, 1996; Stone et al. 1996). In Ohsuga et al. (2005) only the  $r\phi$  component of the viscous stress is included, while the  $\theta\phi$  component is neglected. So our first aim in this paper is to examine the effect of including the  $\theta\phi$  component on the dynamics of the slim disk. It should play an important role in the angular momentum transport between different latitudes and might suppress the Kelvin–Helmholtz instability on the boundary between the outflow regions and the disk.

Another aim is to study the effect of the magnitude of  $\alpha$ . Ohsuga et al. (2005) only consider one value of  $\alpha$ . Previous HD numerical simulations of non-radiative accretion flows have shown that the structure and dynamics of accretion flow depend on the value of  $\alpha$  (Igumenshchev & Abramowicz 1999; Stone et al. 1999; Yuan et al. 2012). The radial profile of inflow rate becomes significantly flatter when  $\alpha$  becomes larger (Yuan et al. 2012). Different than the non-radiative accretion flow, a slim disk is dominated by radiation. It is thus unclear whether or how the dynamics of accretion flow depend on the value of  $\alpha$ .

Yet another aim of the present work, which is perhaps more interesting, is to examine the radial profiles of inflow rate. In almost all analytical models of accretion disks, the mass accretion rate is assumed to be constant with radius. The validity of this assumption, however, has never been proved. For the hot accretion flows, both HD and MHD numerical simulations have found that the mass inflow rate (refer to Equation (4) for definition) decreases inward (e.g., Stone et al. 1999; Stone & Pringle 2001; Yuan et al. 2012, and references therein). This is one of the most important findings of global simulation of accretion flows, because this result supplies an important clue to revealing the dynamics of accretion flow. Various models have been proposed to explain this result such as adiabatic inflow–outflow solution (Blandford & Begelman 1999, 2004; Begelman 2012) and convection-dominated accretion flow (CDAF; Narayan et al. 2000; Quataert & Gruzinov 2000). In the former, it is *assumed* that the inward decrease of inflow rate is because of mass loss in the outflow, while in the latter the flow is assumed to be convectively unstable, and a convective envelope solution is constructed that can also explain the simulations. No outflow is needed in CDAFs. Recent numerical simulations have shown that MHD accretion flows are convectively stable (Narayan et al. 2012; Yuan et al. 2012). Moreover, by comparing the properties of inflow and outflow on the base of their HD and MHD numerical simulation data, Yuan et al. (2012) argue that mass outflow should be significant. They propose that inward decrease of accretion rate is due to outflow. Li et al. (2013) obtained a similar conclusion. In most of the published papers, the inflow and outflow rates (Equation (4) and (5)) are computed at each instant of time by using instantaneous velocities, and then the time-averaged. Narayan et al. (2012; see also Sadowski et al. 2013 for the case of spin black holes), however, found that the outflow rate is much lower since they think the outflow rate should be

calculated by doing the time-average first (see Yuan et al. 2012 for more discussions on the discrepancy of the two approaches of calculating the outflow rate). While it is agreed that outflow exists, so far the strength of outflow is still an open question. F. Yuan et al. (2013, in preparation) have also studied the mechanism of producing outflow. It was found that in the HD case it is buoyancy associated with the convective instability, while it is mainly magnetic centrifugal force in the case of MHD accretion flow. It is obviously interesting to see whether the radial profile of the inflow rate of a slim disk behaves like a hot accretion flow, and if it does, whether the outflow is produced by the buoyancy associated with the convective instability.

The paper is organized as follows. We describe our models and numerical method in Section 2. The simulation results are presented in Section 3. Section 4 is devoted to a summary and discussions.

## 2. MODELS AND NUMERICAL METHOD

The RHD equations are the same as those in Ohsuga et al. (2005). In the RHD equations, the flux-limited diffusion (FLD) approximation developed by Levermore & Pomraning (1981) is adopted. We neglect the self-gravity of the disk and use the pseudo-Newtonian potential to mimic the general relativistic effects,  $\psi = -GM/(r - r_s)$  (Paczynski & Wiita 1980), where  $G$  is the gravitational constant,  $M$  is the mass of the black hole,  $r_s = 2GM/c^2$  the Schwarzschild radius, and  $r$  is the radius. We assume that the gas is in local thermodynamic equilibrium and neglect the frequency dependence of the opacities.

As we state in Section 1, we adopt a stress tensor to mimic the shear stress, which is in reality should be replaced by the magnetic stress associated with MHD turbulence driven by the MRI. In most cases, following Stone et al. (1999), we assume that the only non-zero components of  $T$  are the azimuthal components:

$$T_{r\phi} = \eta r \frac{\partial}{\partial r} \left( \frac{v_\phi}{r} \right), \quad (1)$$

$$T_{\theta\phi} = \frac{\eta \sin(\theta)}{r} \frac{\partial}{\partial \theta} \left( \frac{v_\phi}{\sin(\theta)} \right). \quad (2)$$

Here, the dynamical viscosity coefficient  $\eta$  is described as a function of the pressure  $\eta = \alpha(p_g + \lambda E_0)/\Omega_K$ , where  $\Omega_K$  is the Keplerian angular speed,  $p_g$  is the gas pressure,  $E_0$  is the radiation energy density, and  $\lambda$  is the flux limiter (Levermore & Pomraning 1981). The viscous dissipative function is given by  $(T_{r\phi}^2 + T_{\theta\phi}^2)/\eta$ .

All of our models are calculated in spherical coordinates  $(r, \theta, \phi)$ . The origin is set at a central black hole of  $M = 10M_\odot$ . The size of the computational domain is  $2r_s \leq r \leq 500r_s$  and  $0 \leq \theta \leq \pi$  or  $0 \leq \theta \leq \pi/2$ . The inner boundary ( $r_{\text{in}}$ ) must be smaller than the sonic point of the accretion flow, which ensures that the inner boundary conditions do not affect the simulation results. Abramowicz et al. (1988) show that for a slim disk the location of the sonic point depends on the accretion rate and the viscosity parameter  $\alpha$ . For small  $\alpha$  and a high accretion rate, the sonic point locates in the range of  $(2 - 3)r_s$ . So we set  $r_{\text{in}} = 2r_s$ .

The computational domain is divided into  $N_r \times N_\theta$  grid cells. A non-uniform grid is employed in the  $r$  direction.

TABLE 1  
SUMMARY OF SIMULATIONS

Models	Run	$\alpha$	$\dot{m}_{\text{input}}$	$\theta$	Stress Tensor	$N_r \times N_\theta$	$t_s$ (orbits)	$t_f$ (orbits)	$\dot{m}_{\text{acc}}$	$L$
A	1a	0.1	1000	$0 \sim \pi$	$T_{r\phi}$	$96 \times 225$	11.5	46.1	184.5	2.4
B	1b	0.1	1000	$0 \sim \pi$	$T_{r\phi}, T_{\theta\phi}$	$96 \times 225$	11.5	46.1	160.0	2.2
	2b	0.1	3000	$0 \sim \pi$	$T_{r\phi}, T_{\theta\phi}$	$96 \times 225$	11.5	46.1	374.5	3.2
	3b	0.05	3000	$0 \sim \pi$	$T_{r\phi}, T_{\theta\phi}$	$96 \times 225$	11.5	46.1	382.8	3.6
	4b	0.01	3000	$0 \sim \pi$	$T_{r\phi}, T_{\theta\phi}$	$96 \times 225$	63.5	98.1	240.3	4.2
	5b	0.005	3000	$0 \sim \pi$	$T_{r\phi}, T_{\theta\phi}$	$96 \times 225$	150.0	184.6	125.3	3.6

Note: Columns 1 and 2: the classification of our models and their number, respectively. Column 3: the viscous parameter ( $\alpha$ ). Column 4: the mass injection rate ( $\dot{m}_{\text{input}}$ ) in unit of the critical mass accretion rate,  $\dot{M}_{\text{crit}} \equiv L_{\text{Edd}}/c^2$ . Columns 5, 6, and 7: the computational domain in the  $\theta$  direction, the components of stress tensor, and the quantity of grid cells. Column 8: the approximate time  $t_s$  (in units of the orbital time at  $r=100 r_s$ ) after which the accretion flows become quasi-steady. Column 9: the final time  $t_f$ . Columns 10 and 11: the mass accretion rate on the BH ( $\dot{m}_{\text{acc}}$ ) in unit of the critical mass accretion rate, and the luminosity ( $L$ ) in unit of  $L_{\text{Edd}}$ , respectively.

The grid points in the  $r$  direction are equally distributed logarithmically, i.e.,  $\Delta \ln r = \text{constant}$ . In the  $\theta$  direction, in order to better resolve the flow at the equator and to not lose the resolution at the axis, we adopt the mixed grid. Twenty grids are uniformly distributed within the  $\pi/8$  from the axis, i.e.,  $\Delta\theta = \pi/160$ . Other grids are distributed in the angular range of  $\pi/8 \leq \theta \leq 7\pi/8$  or  $\pi/8 \leq \theta \leq \pi/2$  in such a way that  $\Delta \cos(\theta) = 3\pi/(4(N_\theta - 20))$  or  $3\pi/(8(N_\theta - 20))$ . The outflow boundary condition is adopted at the inner radial boundary, i.e. the values of physical variables in the ghost zones are set to the values at the inner radial boundary. The outer radial boundary condition is the same as that employed by Ohsuga et al. (2005), who suggested that the matter, having a specific angular momentum corresponding to the Keplerian angular momentum at  $r = 100r_s$ , is continuously injected into the computational domain from the outer boundary near the equator. The injected gas distributes within  $0.05\pi$  from the equator in the Gaussian function; their radial velocity is set according to Equation(3.61) in Kato et al. (1998), while their poloidal velocity is set to be zero. In the angular direction, we employ axisymmetry relative to the axis and reflection symmetry relative to the equator (when  $0 < \theta < \pi/2$ ), respectively. The computational domain is initially filled with a hot, rarefied, and optically thin atmosphere. The numerical approach can be found in Ohsuga et al. (2005).

The properties of all of the simulations are listed in Table 1, where Columns 1 and 2 give the classification of our models and their number; Column 3 gives the value of  $\alpha$ ; Column 4 gives the mass injection rate ( $\dot{m}_{\text{input}}$ ) in units of the critical mass accretion rate,  $\dot{M}_{\text{crit}} \equiv L_{\text{Edd}}/c^2$ ; Columns 5, 6, and 7 give the computational domain in the  $\theta$  direction, the components of stress tensor, and the quantity of grid cells, respectively; Column 8 gives the approximate dynamical time  $t_s$  (all times in this paper are reported in units of the orbital time at  $r=100r_s$ ) after which the accretion flows become quasi-steady; Column 9 gives the final time  $t_f$ ; and Columns 10 and 11 give the mass accretion rate onto the black hole ( $\dot{m}_{\text{acc}}$ ) in the units of the critical mass accretion rate and the luminosity ( $L$ ) in the units of  $L_{\text{Edd}}$ , respectively. According to the component of stress tensor and the angular range of computational domain, the simulations are divided into two groups, namely Models A and B. Models A contains only the  $r\phi$  component of stress tensor, while Model B

contains both the  $r\phi$  and  $\theta\phi$  components.

Figure 1 displays a two-dimensional density distribution overlaid with velocity vectors. The top and bottom panels are for  $t=92.541$  orbits of Run 2b and 254.085 orbits of Run 5b, respectively.

### 3. RESULTS

#### 3.1. The Effects of $T_{\theta\phi}$

To investigate the effect of  $T_{\theta\phi}$  on the dynamics of accretion flow, we compare Models A and B. Figure 2 shows the angular structure of time-averaged variables at  $r = 5r_s$  and  $30 r_s$  for Run 1a and Run 1b with  $\dot{m}_{\text{input}} = 1000$ . In this paper, all the time-averaged quantities are obtained by averaging 100 data files within 23 orbits after the accretion flows have achieved the quasi-steady state. In Figure 2, the black solid ( $r = 5r_s$ ) and dashed ( $r = 30r_s$ ) lines correspond to Run 1a while the red solid ( $r = 5r_s$ ) and dashed ( $r = 30r_s$ ) lines correspond to Run 1b. The figure shows obvious differences of the flow structure, especially at the high-latitude region.

The angular profiles of angular velocity ( $v_\phi/(r \sin(\theta))$ ) show that the flow in Run 1a rotates faster than that of Run 1b at the high-latitude region. Close to the equator, the rotation of Run 1a is slightly slower than Run 1b. Because  $T_{\theta\phi}$  transports angular momentum between different latitudes, for Run 1a the angular momentum between different latitudes can not be transported, although the high-latitude flow rotates faster than the low-latitude one. Therefore, it is seen that the angular velocity increases from the equator to almost the axis (although the angular velocity at the rotating axis is set to be zero). When  $T_{\theta\phi}$  is included in Run 1b, the angular momentum can be transported from the quickly rotating flows at high latitude to the slowly rotating flows at low latitude. This is why the discrepancy of the rotation velocity between the equator and the high-latitude region is smaller in Run 1b than in Run 1a. The discrepancy of the rotation velocity at the equator between Run 1a and Run 1b is much smaller than in the high-latitude region, since the density at the high-latitude region is much smaller than in the equator.

The angular profiles of radial velocity ( $v_r$ ) show obvious differences between Run 1a and Run 1b, especially at the high-latitude region. The positive value of  $v_r$  indicates that the flows are outflows, while the negative value indicates the inflow nature of flows. At large radii such as  $\sim 30r_s$ , the high-latitude flow (the flow within

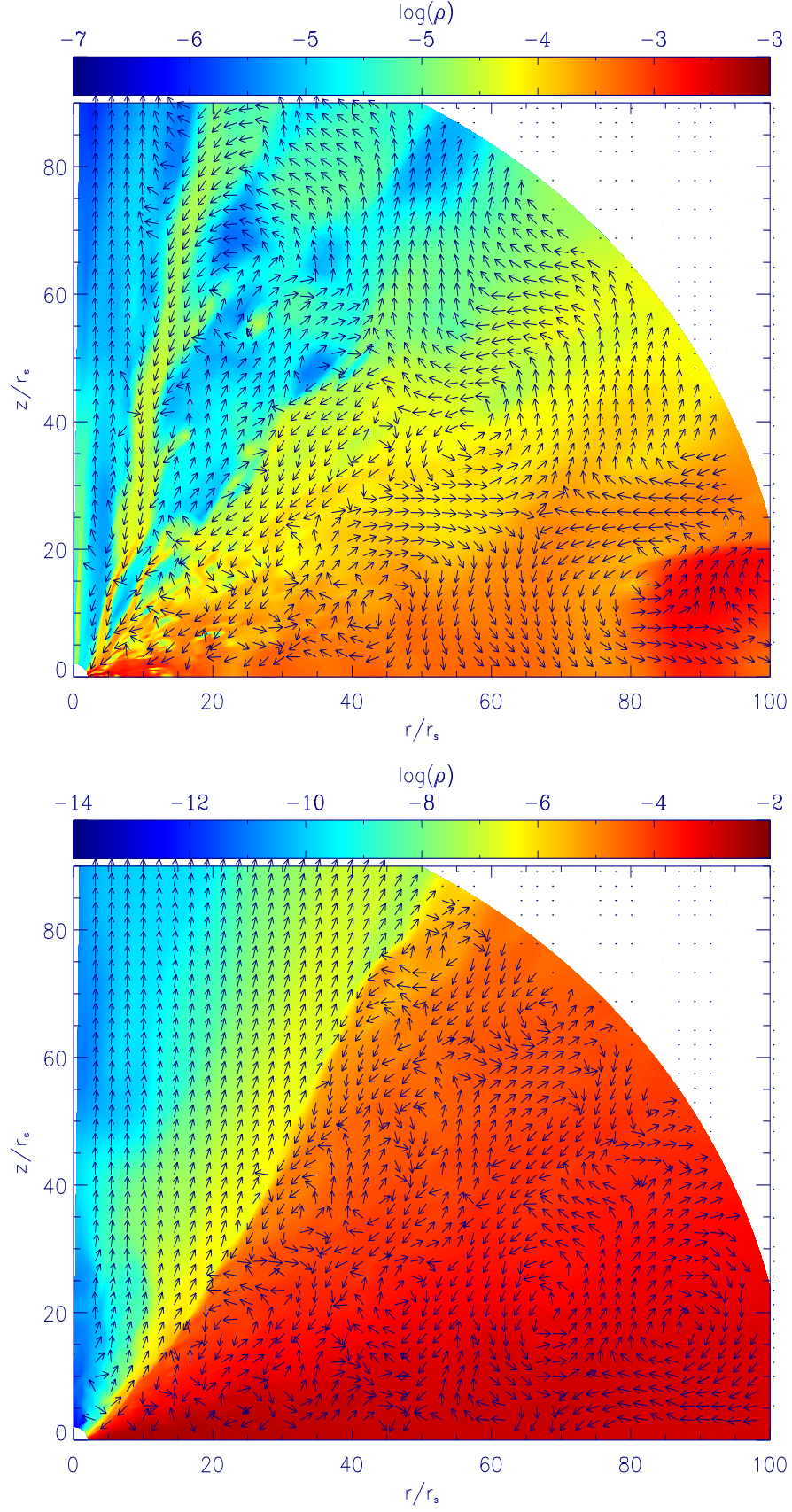


FIG. 1.— Snapshots of the logarithm of density (colors), overlaid with velocity vectors (arrows). Top:  $t = 92.541$  orbits of Run 2b ( $\alpha = 0.1$ ); Bottom: 254.085 orbits of Run 5b ( $\alpha = 0.005$ ).

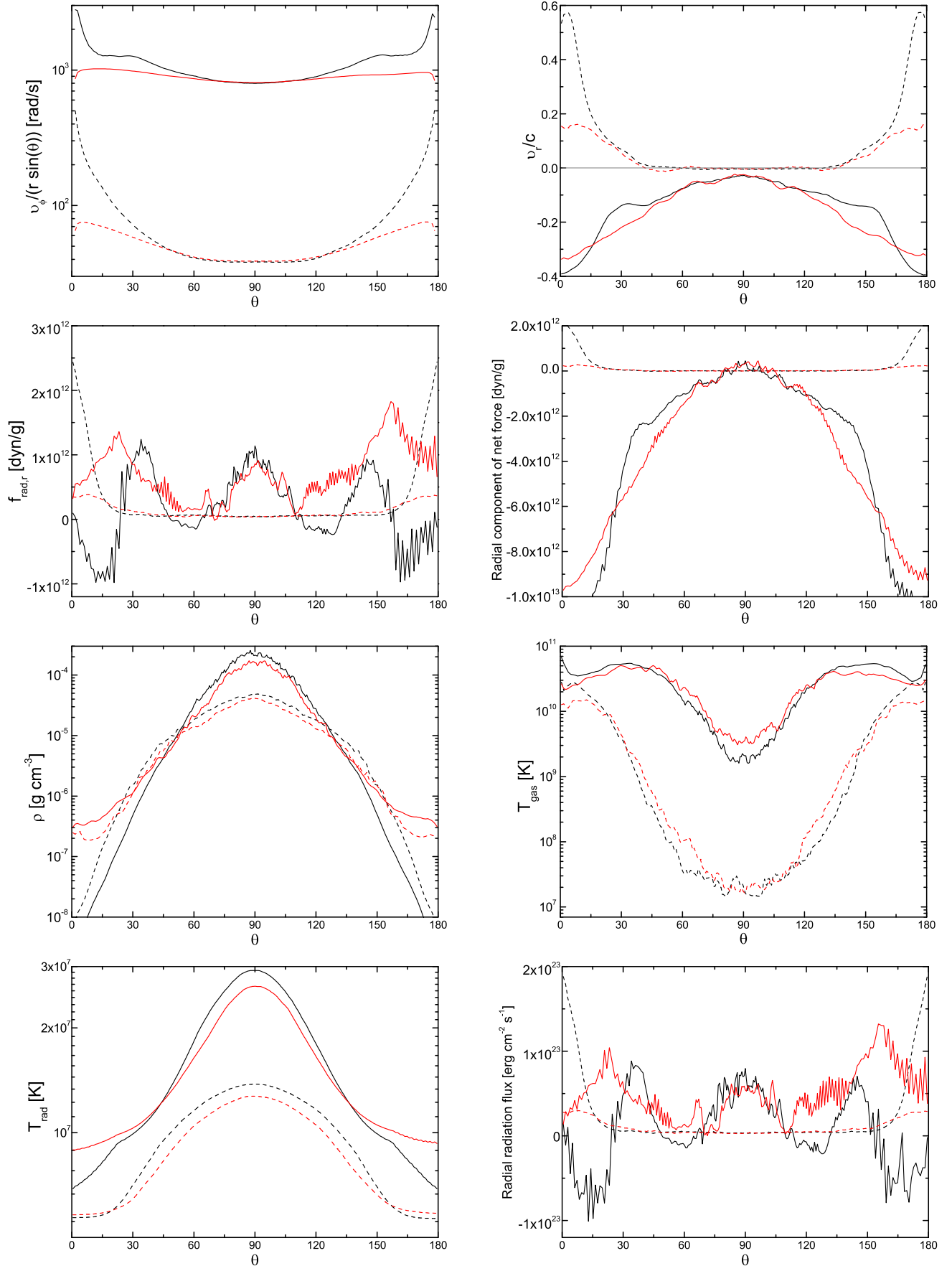


FIG. 2.— Angular profiles of a variety of time-averaged variables for Run 1a ( $T_{\theta\phi} = 0$ ; black) and Run 1b (with  $T_{\theta\phi} \neq 0$ ; red) at  $r=5r_s$  (solid lines) and  $30r_s$  (dashed lines).

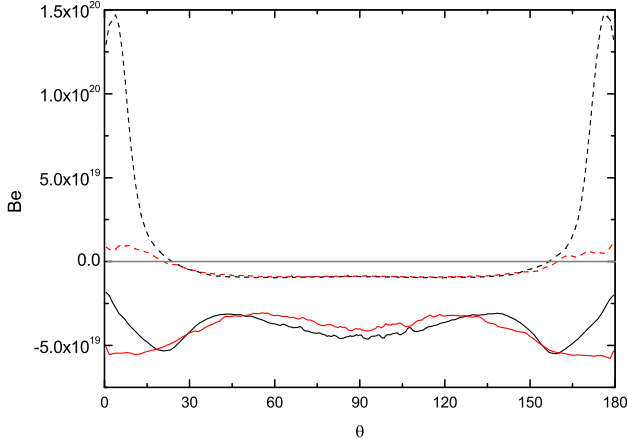


FIG. 3.— Angular profiles of time-averaged Bernoulli parameters for Run 1a ( $T_{\theta\phi} = 0$ ; black) and Run 1b (with  $T_{\theta\phi} \neq 0$ ; red) at  $r = 5r_s$  (solid lines) and  $30r_s$  (dashed lines).

$30^\circ$  from the axis) is mainly outflow. The speed of the high-latitude outflow of Run 1a is higher than that of Run 1b. At small radii such as  $r < 5r_s$ , the flow is inflow at all latitudes for both models. The angular profiles of radial velocity agree with the angular profiles of radial forces, as shown in Figure 2. The radial radiation force dominates the radial component of net force at the high-latitude region at  $\sim 30r_s$ ; therefore, it is the dominant force changing the angular distribution of the radial velocity there. At small radii, gravity is the dominant force.

The angular profiles of density ( $\rho$ ) of Run 1a and Run 2b are similar, with the maximum density located at the equator. Compared with Run 1a, the density of the high-latitude region of Run 1b is higher, while at the equator is slightly lower. The angular profiles of gas temperature ( $T_{\text{gas}}$ ) show that the disk of Run 1a and Run 1b has nearly the same gas temperature at  $30r_s$ . For Run 1b the gas temperature of high-latitude outflow is lower than that of Run 1a. For the high-latitude outflow, the lower the gas temperature, the higher the density.

The angular profiles of the “radiation” temperature ( $T_{\text{rad}} \equiv (E_0/a)^{1/4}$ , where  $a$  is the radiation constant) show that compared with Run 1a, the radiation temperature for Run 1b is lower near the equator and higher near the rotating axis. For the super-critical accretion flow, the radiation force (including also the gradient of the radiation pressure) is the dominant force driving the high-latitude outflow. The radiation force acting on unit mass is given by  $f = \frac{\chi}{c\rho} F_0$ , where the flux-mean opacity  $\chi$  is the sum of components due to absorption and scattering. The scattering in the high-latitude outflow is the dominant factor for the opacity so that  $\chi \propto \rho$  and  $f \propto F_0$ . Here we employ the approximation and have  $F_0 = -\frac{c\lambda}{\chi} \nabla E_0$ . In the optically thin limit,  $|F_0| = cE_0$ . In general, the high-latitude outflow has high gas temperature and low density, so the flow is optically thin. For Run 1a, the opacity of outflow near the rotating axis is close to the optically thin limit, while for Run 1b the opacity of outflow is away from the optically thin limit because of the higher density. Therefore, although Run 1a has lower radiation energy density at the high-latitude region than Run 1b, the radiation flux of Run 1a is larger than that of Run 1b, which is shown by the angular pro-

files of radial radiation flux in Figure 2. Therefore, at the high-latitude region the radiative force of Run 1a is larger, exceeding that of Run 1b. Compared with Run 1a, the density of high-latitude outflow for Run 1b is higher so that the driving force of high-latitude outflow is weaker.

For the strict steady state and for inviscid hydrodynamic flow, the Bernoulli parameter  $Be$  ( $Be \equiv v^2/2 + \gamma p/(\gamma-1)\rho - GM/(r-r_s)$ ) is conserved along the streamline. Therefore, the positive sign of  $Be$  is often used to be the necessary condition for the outflow to escape to infinity. However, in our case, these conditions are not satisfied, thus  $Be$  is no longer conserved (e.g., Yuan et al. 2012). In fact, the initial result from our ongoing work indicates that  $Be$  can increase along the trajectory of outflow elements (F. Yuan et al. 2013, in preparation). This means that an outflow with a negative  $Be$  can also potentially escape to infinity. Despite these uncertainties, we still show in Figure 3 the angular distribution of the time-averaged Bernoulli parameter  $Be$  because its value may still play some role in determining the properties of outflow. We can see that at the region close to the axis ( $\theta < 25^\circ$ ) and  $r = 30r_s$ , the value of  $Be$  in Run 1b is about one order of magnitude lower than that in Run 1a. From Figure 2, we can see that including  $T_{\theta\phi}$  for the polar outflows, rotational speed, radial speed and temperature decrease can decrease the specific  $Be$  of outflow. In general, the value of  $Be$  is larger close to the axis. When compared with the hydro and MHD numerical simulations of hot accretion flow presented in Yuan et al. (2012), it is interesting to note that the angular distribution of  $Be$  is more similar to the MHD case (their Model D in Yuan et al. (2012)) rather than to the hydro case (their Models A, B, and C). This is perhaps because the radiation acceleration in the  $r$  direction is much stronger in the region close to the axis than in other directions. In the case of Models A, B, C in Yuan et al. (2012), there is no such force. But in the MHD case, the magnetic pressure force plays a similar role with the radiation force here.

### 3.2. The Effect of the Viscous Parameter $\alpha$

Figure 4 shows the angular distribution of the time-averaged flow for Model B (with  $\dot{m}_{\text{input}} = 3000$ ; i.e., Run 2b and 5b) at  $r = 5r_s$  and  $r = 30r_s$ , respectively. We can see that the viscosity parameter  $\alpha$  obviously affects the angular distribution of accretion flow. The angular profiles of angular velocity ( $v_\phi/(r\sin(\theta))$ ) show a large difference close to the axis because of the different  $\alpha$ . When  $\alpha$  is smaller, the flow rotates faster. A smaller  $\alpha$  results in a smaller  $T_{\theta\phi}$ ; thus, the angular momentum cannot be efficiently transported from high to low latitudes. The angular profile of the radial velocity ( $v_r/c$ ) is different for different  $\alpha$ . The speed of the high-latitude outflow in Run 15b is higher than that of Run 2b. At  $r = 30r_s$ , the high-speed outflow is constrained to be within  $30^\circ$  from the axis. With the decrease of  $\alpha$ , the range of  $\theta$  within which high-latitude outflow takes place becomes larger toward the equator. At  $r = 5r_s$ , the radial velocity is negative over most  $\theta$ .

The plots of angular profiles of density, gas temperature, and “radiation” temperature show that these three quantities change rapidly with  $\theta$  for Run 5b. With the decrease of  $\alpha$ , the density and radiation energy den-



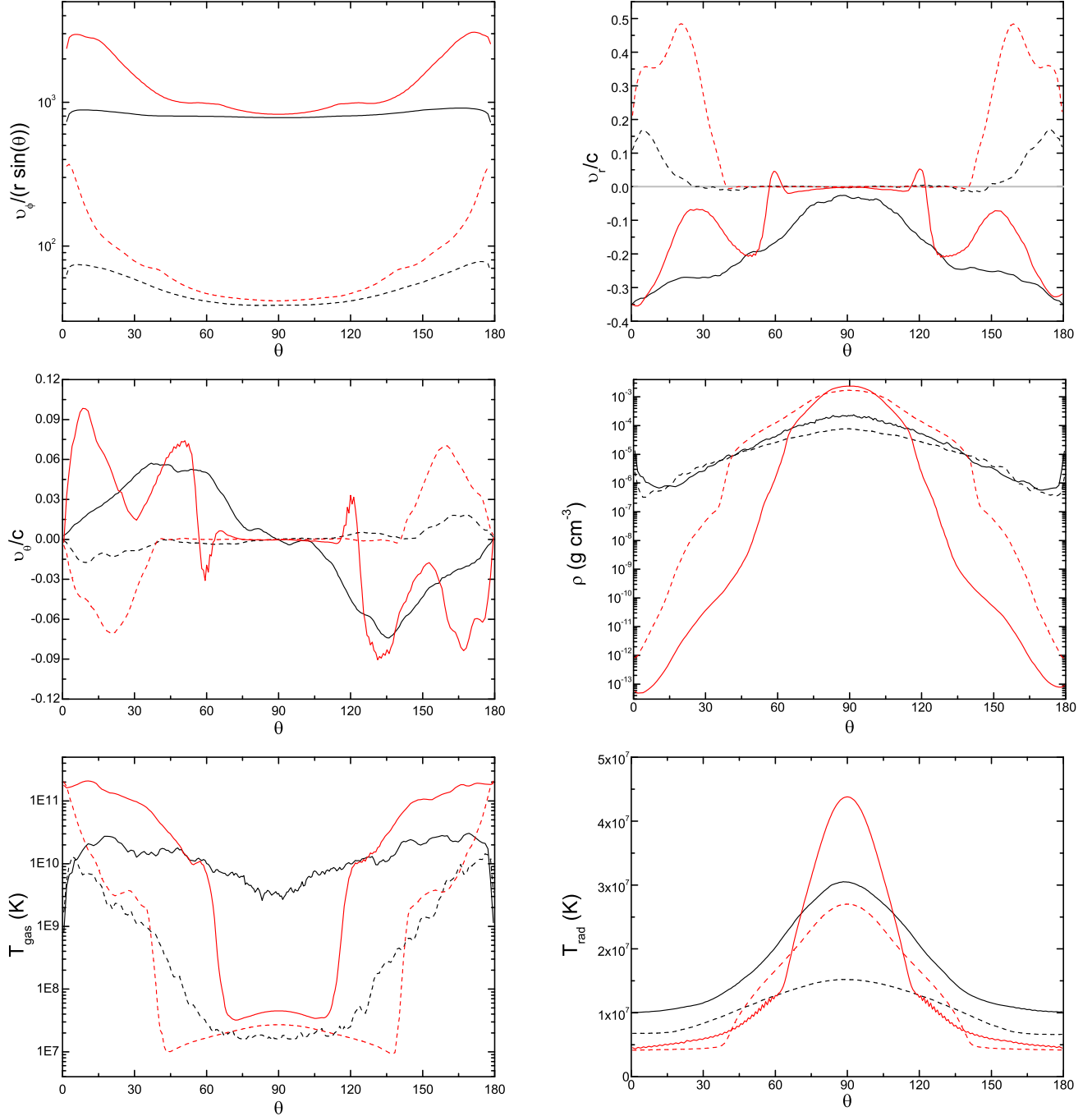


FIG. 4.— Angular profiles of a variety of time-averaged variables from Run 2b ( $\alpha = 0.1$ ; black) and Run 5b ( $\alpha = 0.005$ ; red) at  $r = 5r_s$  (solid lines) and  $30r_s$  (dashed lines).

sity concentrate toward the equator, and the flow can be divided into two areas with different temperature, i.e., a low-temperature area near the equator and a high-temperature area near the axis.

In order to understand the angular profiles of radial velocity, we plot in Figure 5 the angular distribution of radial forces acting on unit mass for Run 5b at  $r = 5$  (top panel) and  $30r_s$  (bottom panel), respectively. We can see that the angular distribution of net force (solid lines) is similar to the angular distribution of  $v_r$  shown in Figure 4. In addition, Figure 5 shows that within  $10^\circ < \theta < 90^\circ$  the radial component of centrifugal force efficiently

counteracts the gravity and even exceeds the gravity at some degree. The top panel shows that the flows within  $30^\circ$  from the equator are super-Keplerian at  $30r_s$ . At  $r \sim 10r_s$ , the flows are super-Keplerian within  $40^\circ$  from the equator. However, within  $\sim 20^\circ$  from the axis, the radial component of centrifugal force rapidly decreases and cannot efficiently counteract the gravity. Hence, the equivalent potential well is deeper near the axis than near the equator. On the other hand, the radial component of the gas-pressure gradient force is negligible within  $60^\circ$  of the equator, while near the axis this component is not negligible but is not the dominant force. The radial net

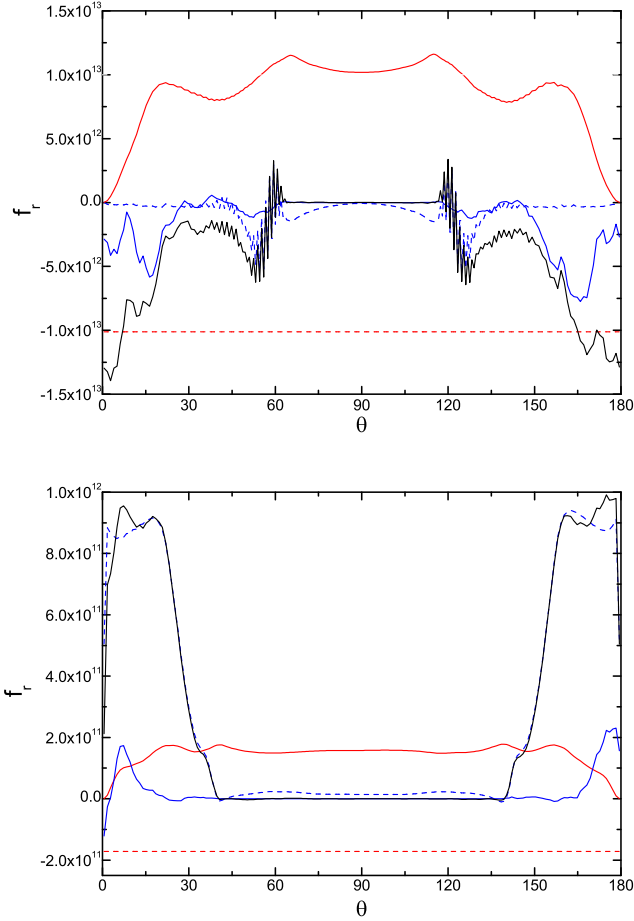


FIG. 5.— Angular distribution of the radial forces per unit mass for Run 5b at  $r = 5r_s$  (top panel) and  $30r_s$  (bottom panel). The radial forces include gravity (red dashed line), centrifugal force (red solid line), radiation force (blue dashed line), gas-pressure gradient force (blue solid line), and their sum (black solid line).

force within  $60^\circ$  of the equator is dominated by the radial radiation force, the gravity, and the radial centrifugal force. In the inner region, the radial net force near the axis is dominated by the gravity, so that we see that there is inflow near the axis. In the outer region, the radial net force near the axis is dominated by the radial radiation force, so that we can see that there is strong outflow near the axis. Hence, the radial radiation force plays an important role in maintaining the radial equilibrium of flows near the equator and driving the high-latitude outflow in the outer region.

Figure 6 shows the angular distribution of angular forces. It is seen that the angular component of net force is nearly zero near the equator, which indicates that flows are in force equilibrium near the equator. This is because that the angular component of gas-pressure gradient force is also negligible, and the radiation force balances the centrifugal force in the  $\theta$ -direction. The angular motion of flows near the axis is controlled by the centrifugal force and gas-pressure gradient force, while the angular component of radiation force is negligible near the axis.

### 3.3. Radial Structure of Accretion Flows

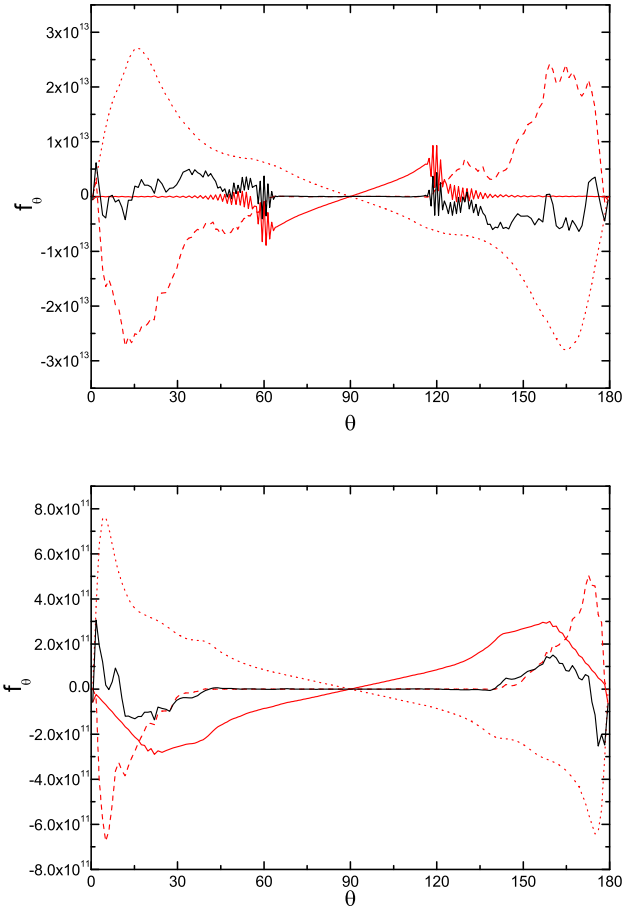


FIG. 6.— Angular distribution of the angular forces per unit mass for Run 5b at  $r = 5r_s$  (top panel) and  $30r_s$  (bottom panel). The angular forces include the angular component of radiation force (red solid line), centrifugal force (red dotted line), gas-pressure gradient force (red dashed line), their sum (is shown by the black solid line).

The radial structure of a slim disk has been solved using a vertical-integrated one-dimensional method (e.g., Abramowicz et al. 1988). However, the solution is one dimensional, thus the method cannot treat more viscous components besides  $T_{r\phi}$  and cannot address outflow. Here, on the basis of the solution of two-dimensional simulation, we plot the radial structure of the time-averaged flow near the equator in Figure 7. The solution is averaged over the angle between  $\theta = 84^\circ$  and  $\theta = 96^\circ$ . In Figure 7, the left panel is for Run 2b (red line) and Run 3b (blue line), while the right panel is for Run 4b (red line) and Run 5b (blue line).

Panel (A) of Figure 7 shows the radial profiles of density. The dot-dashed lines indicate the self-similar solution of the slim-disk model (Wang & Zhou 1999). We find that the density profile of different models can be well described by a power law function,  $\rho(r) \propto r^{-p}$  with  $p \approx 0.55$ . This result is much flatter than the self-similar solution of the slim disk where  $\rho(r) \propto r^{-1.5}$  (Wang & Zhou 1999), but it is very similar to the case of hot accretion flows (Stone et al. 1999; Yuan et al. 2012, and references therein). The reason for the discrepancy is that in the self-similar solution the mass accretion rate  $\dot{M}(r)$  is assumed to be a constant of radius, while as



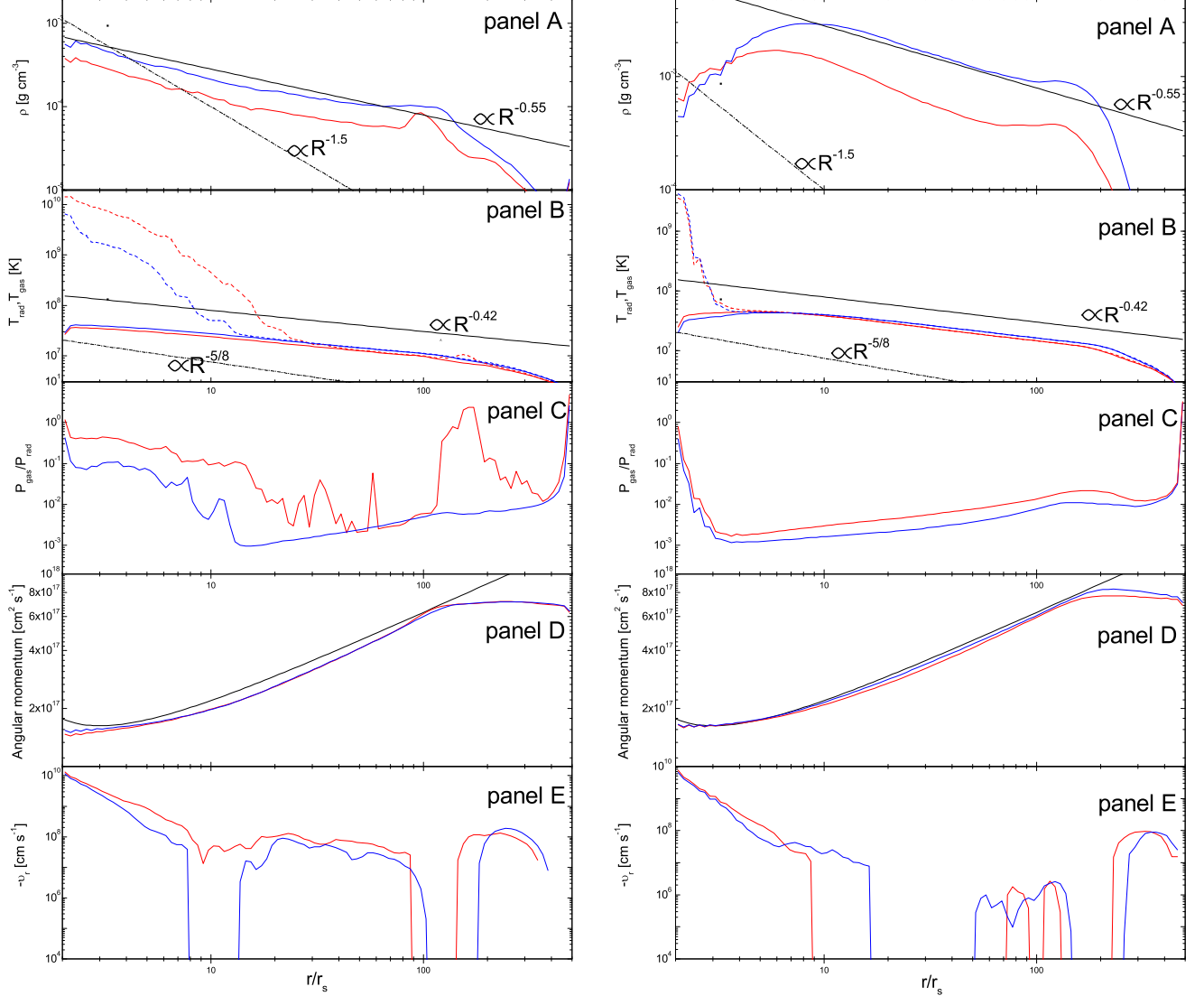


FIG. 7.— Radial structure of some time-average quantities. The left panel is for Run 2b ( $\alpha = 0.1$ ; red line) and Run 3b ( $\alpha = 0.05$ ; blue line), while the right panel is for Run 4b ( $\alpha = 0.01$ ; red line) and Run 5b ( $\alpha = 0.005$ ; blue line). The plots from top to bottom are for density, gas and radiation temperature, the ratio of gas pressure to radiation pressure, specific angular momentum, and radial velocity, respectively. The dot-dashed lines denote the profile of the one-dimensional solution. The black solid line is to guide our eyes. In panel (D), the black solid line indicates the Keplerian angular momentum.

we will show in Section 3.4, the accretion rate actually decreases inward because of the mass loss in outflows. Moreover, it is interesting to note that the value of power law index of the density profile,  $p$ , is quite “universal” for different models, although these models have different  $\alpha$  and different radial profiles of inflow rate (refer to Section 3.4). Bu et al. (2013) studied the effects of initial and boundary conditions in simulations of accretion flow. They find a similar result, namely the density profile is more converged compared with the diverse radial profile of inflow rate.

Our result is apparently different from Figure 11 in Ohsuga et al. (2005), in which they find  $\rho(r) \propto r^{-1.5}$ . For comparison with Ohsuga et al. (2005), we have checked the models in Ohsuga et al. (2005) and found that only when  $\dot{m}_{\text{input}} = 500$  and 1000, and  $\alpha = 0.1$ , the density profile can be described by  $\rho(r) \propto r^{-1.5}$ . All other models have  $\rho(r) \propto r^{-0.55}$ . Moreover, in the former case, the  $\rho(r) \propto r^{-1.5}$  density profile only holds

in the range of  $r \lesssim 30r_s$ . Beyond this radius, the profile becomes much flatter. But in the latter case, the  $\rho(r) \propto r^{-0.55}$  density profile holds until  $r \sim 80r_s$ , as shown by Figure 6. The reason for the discrepancy is unclear.

Panel (B) of Figure 7 shows the radial profiles of gas temperature  $T_{\text{gas}}$  (red and blue dashed lines) and “radiation” temperature  $T_{\text{rad}}$  (red and blue solid lines).  $T_{\text{rad}}$  can be approximately described by a radial power law function of  $T_{\text{rad}} \propto r^{-0.42}$ , as the black solid line shows. This is again flatter than the self-similar solution of the slim-disk model, which has  $T_{\text{rad}} \propto r^{-5/8}$  as shown by the dot-dashed line. We think the reason is because the compression work becomes weaker because of the presence of outflow. In the inner region close to the black hole,  $T_{\text{rad}}$  becomes flatter. We can find that  $T_{\text{gas}}$  and  $T_{\text{rad}}$  are nearly equal in the outer region, while the gas temperature is higher than  $T_{\text{rad}}$  in the inner region. The radius where the two temperatures deviate depends on

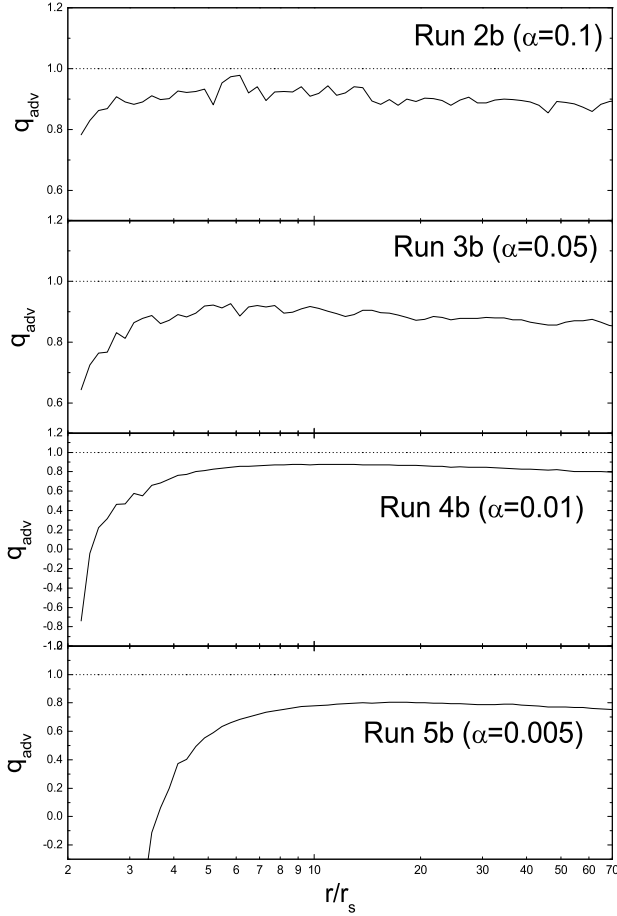


FIG. 8.— Time-averaged advection factor  $q_{\text{adv}}$  (cf. Equation (3)) near the equator for the models of  $\dot{m}_{\text{input}} = 3000$ . The solution is averaged over an angle between  $\theta = 84^\circ$  and  $\theta = 96^\circ$ . Dotted lines indicate  $q_{\text{adv}}=1$ .

the mass-injection rate and viscous parameter  $\alpha$ . The higher the mass-injected rate and the smaller the  $\alpha$ , the smaller the “deviation” radius. However, when  $\alpha = 0.01$  and  $0.005$ , the “deviation radius” is located around the inner boundary. The discrepancy of the two temperatures is because of the inefficient coupling between gas and radiation. The energy transfer between gas and radiation is controlled by the absorption opacity  $\kappa_p$  (refer to the term  $|4\pi\kappa_p B - c\kappa_p E_0|$  ( $B$  is the blackbody radiation intensity) of Equations (7) and (8) in Ohsuga et al. 2005). The absorption opacity  $\kappa_p \propto \rho^2 T_{\text{gas}}^{-7/2}$  is due to free-free absorption and bound-free absorption. We find  $\kappa_p \propto r^{0.37}$ , i.e.,  $\kappa_p$  decreases inward. Therefore, at a small radius, the coupling between radiation and gas is weak, and the temperature equilibrium between the gas and the radiation field is not achieved before the gas falls onto the black hole. Smaller  $\alpha$  gives rise to smaller radial velocity, which provides more time to transfer the energy of the gas to the radiation field. So, the “deviation radius” moves inward with the decrease of  $\alpha$ .

Panel (D) in Figure 7 shows the radial distribution of the specific angular momentum. We can see that  $\alpha$  can affect the angular momentum distribution, especially in the vicinity of the black hole ( $r < 10r_s$ ). In the case of

$\alpha=0.01$  and  $0.005$ , the specific angular momentum becomes super-Keplerian in the range of  $3-6 r_s$ .  $\dot{m}_{\text{input}}$  also affects the angular momentum distribution. The models with smaller  $\alpha$  and lower  $\dot{m}_{\text{input}}$  have slightly flatter distribution. This result does not agree with that of Abramowicz et al. (1988). Abramowicz et al. (1988) identified the tendency of the specific angular momentum distribution to become flatter with the increase of the accretion rate when the accretion rate is less than  $800\dot{M}_{\text{crit}}$ . They could not study the higher accretion rate, because their method fails for  $\dot{M} > 800\dot{M}_{\text{crit}}$ . The reason for the discrepancy is unclear.

To analyze the energetics of all the models, we define the advection factor ( $q_{\text{adv}}$ ) of accretion flow as follows:

$$q_{\text{adv}} \equiv \frac{Q_{\text{adv}}}{Q_{\text{vis}}} = 1 - \frac{Q_{\text{rad}}^-}{Q_{\text{vis}}}, \quad (3)$$

where  $Q_{\text{adv}}$  is the gas and radiation energy advection rate,  $Q_{\text{vis}} = T^2/\eta$  is the viscous dissipation rate, and  $Q_{\text{rad}}^-$  is the radiation cooling rate. Here  $Q_{\text{rad}}^-$  is defined as the  $\theta$  component of  $-\nabla \cdot F$  ( $F$  is the radiation flux). Both  $Q_{\text{rad}}^-$  and  $Q_{\text{vis}}$  are obtained first by time-averaging and then by averaging the quantity over an angle between  $\theta = 84^\circ$  and  $\theta = 96^\circ$ . Figure 8 shows the time-averaged advection factor near the equator for the models of  $\dot{m}_{\text{input}} = 3000$  (i.e., Runs 2b, 3b, 4b, and 5b). We can see that  $q_{\text{adv}}$  is approximately close to a constant in the range of  $(5-70)r_s$ . The value of  $q_{\text{adv}}$  decreases inward when  $r < 10r_s$ , especially for the models with small  $\alpha$ . Since the opacity of accretion flow is dominated by scattering opacity and the half-thickness of accretion decreases inward, the vertical opacity of accretion flow decreases inward. Therefore, the photon trapping effect becomes weaker and the radiation becomes stronger.  $Q_{\text{rad}}^-$  can even be larger than  $Q_{\text{vis}}$ , so  $q_{\text{adv}}$  is negative, as shown by Figure 8. This is consistent with Abramowicz et al. (1988). This indicates that advection plays a heating rather than cooling role, similar to the case of luminous hot accretion flows (Yuan 2001).

#### 3.4. Inflow and Outflow: Rates and Properties

Following Stone et al. (1999), we define the mass inflow ( $\dot{m}_{\text{in}}$ ) and outflow rates ( $\dot{m}_{\text{out}}$ ), in units of the critical mass accretion rate  $\dot{M}_{\text{crit}}$ , as the following time-averaged and angle-integrated quantities:

$$\dot{m}_{\text{in}}(r) = -\frac{c^2}{L_{\text{Edd}}} \int_0^\pi 2\pi r^2 \rho \min(v_r, 0) \sin\theta d\theta, \quad (4)$$

$$\dot{m}_{\text{out}}(r) = \frac{c^2}{L_{\text{Edd}}} \int_0^\pi 2\pi r^2 \rho \max(v_r, 0) \sin\theta d\theta. \quad (5)$$

The net mass accretion rate,  $\dot{m}_{\text{net}}(r) = \dot{m}_{\text{in}}(r) - \dot{m}_{\text{out}}(r)$ , is the accretion rate that finally falls onto the black hole. It is noted that the above rates are obtained by time-averaging the integral rather than integrating the time-averages. According to Equation (5), we know that the outflow rate is not a correct measurement of real outflow, although it can provide some important information. This is because it includes the contribution of turbulent motion.

Figure 9 shows the radial distribution of inflow, outflow, and net rates of Model B ( $\dot{m}_{\text{input}} = 3000$ ; i.e., Runs

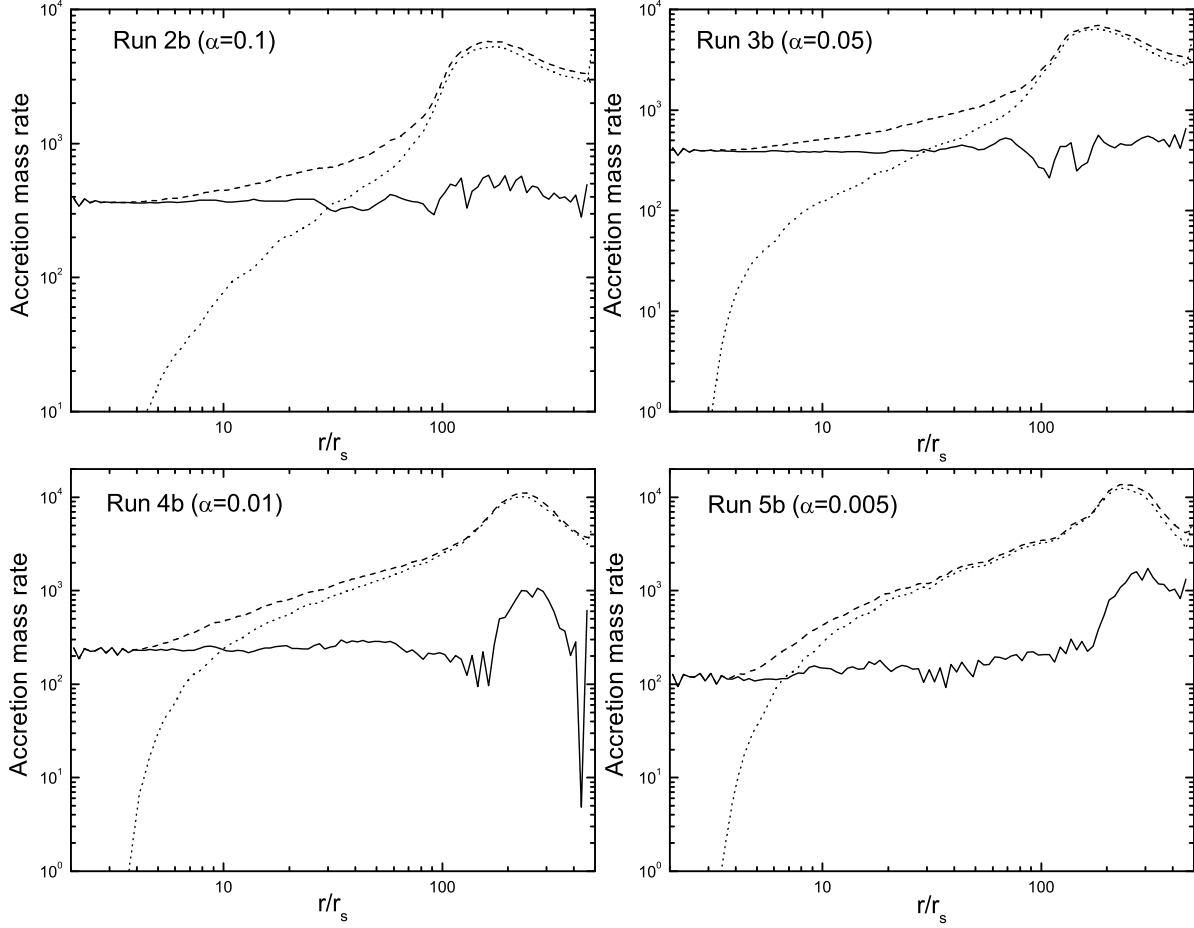


FIG. 9.— Radial profiles of inflow (dashed line), outflow (dotted line), and net rates (solid line) of Model B for various  $\alpha$ . This result is very similar to the case of hot accretion flows, see text for details.

2b, 3b, 4b, and 5b). We can see that the inflow and outflow rates decrease inward, as in the case of hot accretion flows (Stone, Pringle et al. 1999; Yuan et al. 2012, and references therein). The radial profiles of  $\dot{m}_{\text{in}}$  and  $\dot{m}_{\text{out}}$  can be described by a power law function of radius. Using  $\dot{m}_{\text{in}}(r) \propto r^s$  to fit the inflow rate in the range of  $(8 - 50)r_s$ , we find that the value of  $s$  is not sensitive to  $\dot{m}_{\text{input}}$  but mainly determined by the value of  $\alpha$ . A large  $\alpha$  corresponds to a small  $s$ . We have calculated models with different  $\dot{m}_{\text{input}}$  and derived the average values of  $s$ . They are  $\sim 0.37, 0.44, 0.76$ , and  $0.98$  for models with  $\alpha = 0.1, 0.05, 0.01$ , and  $0.005$ , respectively. The dependence of  $s$  on  $\alpha$  can be approximately described by a power law function  $s \propto \alpha^{-0.33}$ . This result is again similar to the case of hot accretion flows. Yuan et al. (2012) find that  $s \sim 0.54$  and  $0.65$  for  $\alpha = 0.01$  and  $0.001$ , respectively. Note that the definition of  $\alpha$  is different in the two works. We find that the value of  $\alpha$  in this paper corresponds to a smaller  $\alpha$  in Yuan et al. (2012). The quantitative comparison of the value of  $\alpha$  is difficult. As argued in Yuan et al. (2012) and F. Yuan et al. (2013, in preparation), in the case of hot accretion flow, the inward decrease of inflow rate is due to mass loss via outflows. We believe this is also the case for the slim disk. The similar slope in the slim disk and hot accretion flow implies

that the strength of outflow is similar in the two cases. We will discuss the possible origin of outflow below.

In order to analyze the angular distribution of the mass accretion rate, we time-average the following inflow and outflow rates as a function of  $\theta$ :

$$\dot{m}_{\text{in}}(\theta) = -2\pi r^2 \rho \min(v_r, 0) \sin\theta \Delta\theta \frac{c^2}{L_{\text{Edd}}}, \quad (6)$$

$$\dot{m}_{\text{out}}(\theta) = 2\pi r^2 \rho \max(v_r, 0) \sin\theta \Delta\theta \frac{c^2}{L_{\text{Edd}}}. \quad (7)$$

Similar to Equation (5), Equation (7) also does not correctly measure the angular distribution of real outflow. The results are shown in Figure 10 for Model B. We can see that their angular distributions are nearly symmetric to the equator and become broader with the increase of radius and/or  $\alpha$ . The distribution is different than the case of hot accretion flows (refer to Figures 2 and 3 in Yuan et al. 2012). Firstly, in the case of slim disks, the inflow and outflow rates are “synchronous”, i.e., they reach their maximum at the same  $\theta$  angle. But in the case of hot accretion flows, they are not (compare Figure 10 in the present paper and Figures 2 and 3 in Yuan et al. 2012). Secondly, the outflow rate centers around the equatorial plane in the present case, while in the case of

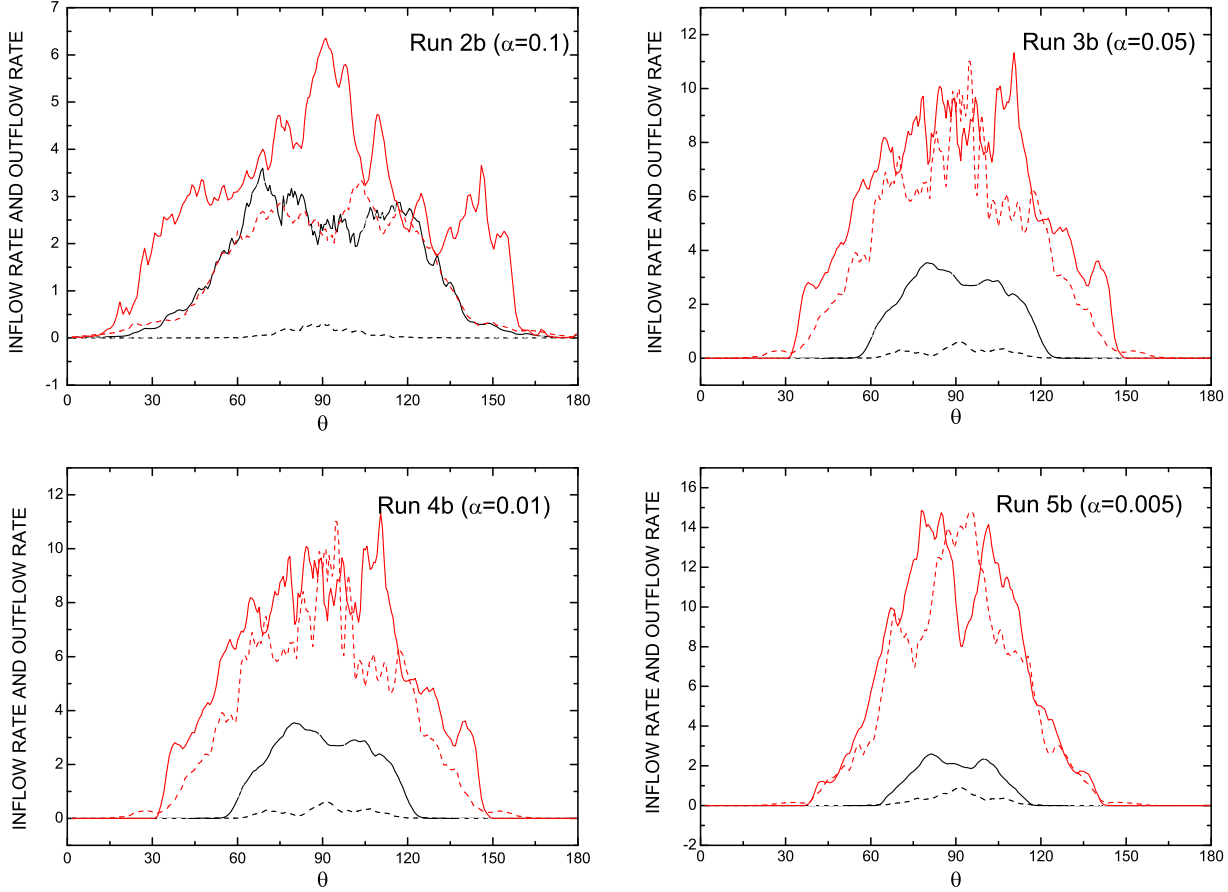


FIG. 10.— Angular distribution of inflow (solid lines) and outflow (dashed lines) rates of Model B. The black and red lines are for  $r = 5r_s$  and  $r = 30r_s$ .

hot accretion flows, the maximum of outflow rate is located roughly at the surface of the disk (their Model B and Model C). In that case, the inflow and outflow rates are not symmetric to the equatorial plane. The reason for the discrepancy is unclear. The outflow becomes stronger with the increase of radius. This is consistent with Figure 9 and is easy to understand. Compared with the region around the equator, the inflow and outflow rates are almost negligible at the high-latitude region, where the radial velocity of outflow is very high. This is because the density of high-latitude flows is very low. The high-latitude outflow is likely driven by radiation, but its contribution to outflow rate seems to be negligible. The outflow rate is dominated by the low-latitude outflow. The nature of the low-latitude outflow, namely whether they are real systematic outflow or simply turbulence, is an important question and needs to be studied in the future. Another question is whether the origins of outflow are real. In the case of hot accretion flows, Yuan et al. (2012) identify the mechanism of producing the outflow by buoyancy when magnetic field is absent. This is because a hydro accretion flow is convectively unstable. In Section 3.5 of the present paper, we analyze the convective stability of slim disks.

Following Yuan et al. (2012), we analyze some properties of inflow and outflow, such as the Bernoulli parameter, gas temperature, radial velocity, and angular momentum. The motivation is to study the mechanism of

producing outflow. We calculate the flux-weighted quantities (refer to Equations (8) and (9) in Yuan et al. 2012) and then time-average the quantities. Figure 11 shows the radial distribution of flux-weighted quantities ( $Be$  in units of  $v_k^2$ , where  $v_k$  is the Keplerian velocity;  $T_{\text{gas}}$  in units of the virial temperature  $T_{\text{vir}} \equiv \frac{GMm_p}{3kr}$ , where  $m_p$  is the photon mass and  $k$  the Boltzmann constant; and  $v_r$  in unit of  $v_k$ ) of inflow and outflow for Run 2b and Run 5b, respectively. In both models,  $Be$  is negative. The value of  $Be$  is in general smaller than that of hot accretion flows (Yuan et al. 2012), which is of course because the energy loss in slim disk is stronger.

The top right panel in Figure 11 shows that the temperature of outflow is higher than that of inflow. This seems to suggest that the mechanism of outflow production is because of buoyancy, like in the case of hydrodynamical hot accretion flow. Moreover, the discrepancy of the two temperatures is larger when  $\alpha$  is larger (Run 2b). The convective stability of slim disk is analyzed in Section 3.5. The bottom left panel in Figure 11 shows that the radial velocity of outflow can be well described by  $v_r/v_k \sim \text{const}$ . This is similar to hot accretion flows (Yuan et al. 2012). It is interesting to note that when  $\alpha$  is smaller, the radial velocities of both inflow and outflow are smaller. For inflow, this is easy to understand. For outflow, the discrepancy of the radial velocity may be related to the discrepancy of the temperature between inflow and outflow. As we can see from the top right

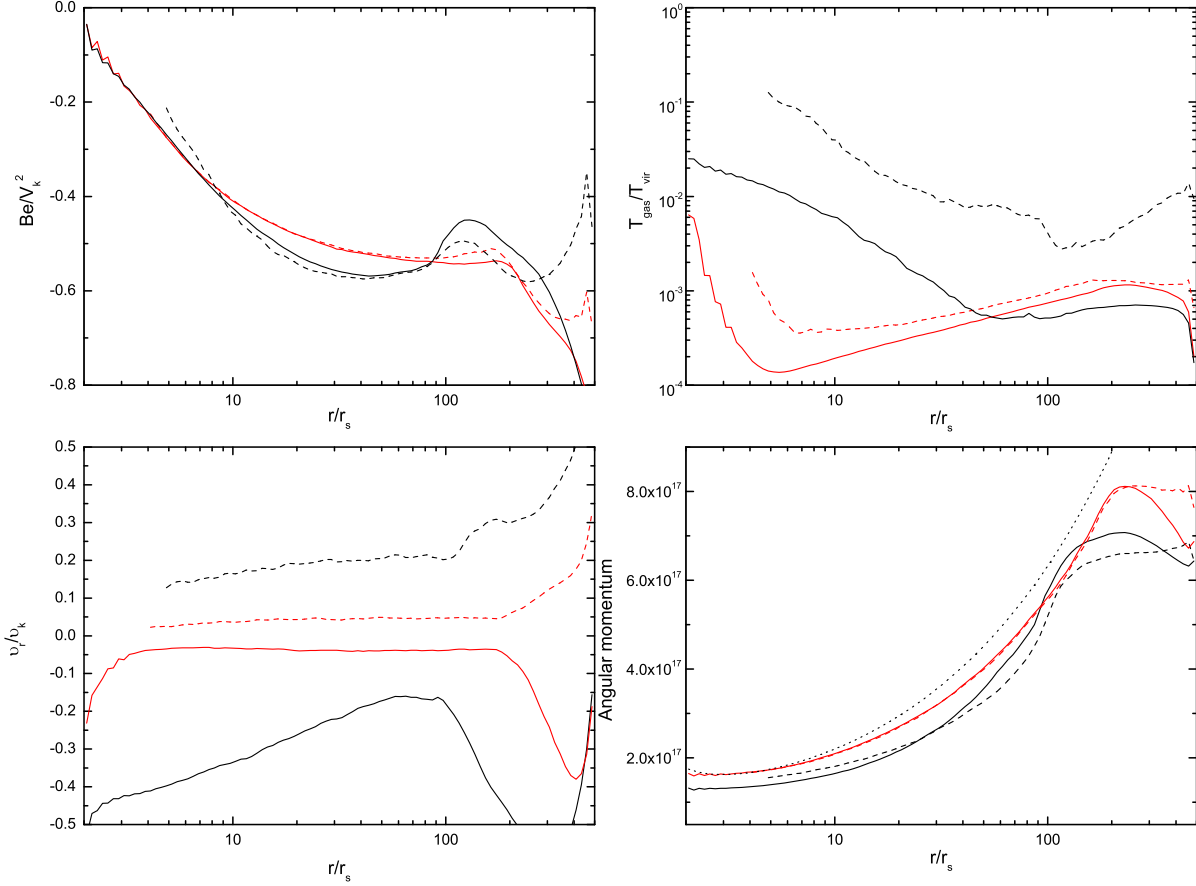


FIG. 11.— Radial distribution of time-averaged values of flux-weighted  $Be$  (in units of  $v_k^2$ ),  $T_{\text{gas}}$  (in units of  $T_{\text{vir}}$ ),  $v_r$  (in unit of  $v_k$ ), and specific angular momentum. The solid and dashed lines are for inflow and outflow, respectively. The black and red lines are for Run 2b ( $\alpha = 0.1$ ) and Run 5b ( $\alpha = 0.005$ ), respectively. The dotted line in the bottom right panel denotes the Keplerian angular momentum at the equator.

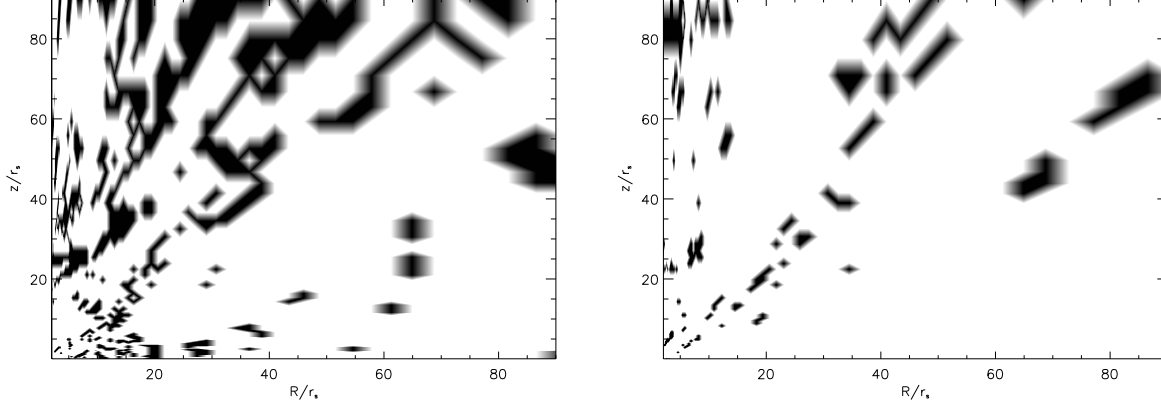


FIG. 12.— Convective stability analysis of Run 2b ( $\alpha = 0.1$ ; left) and Run 5b ( $\alpha = 0.005$ ; right) at  $t = 69.233$  and  $230.776$  orbits, respectively. The dark region denotes negative  $N_{\text{eff}}^2$ , i.e., convectively unstable region.

panel, when  $\alpha$  is smaller, the discrepancy is smaller, and thus the buoyancy may be weaker. The reason why the temperature discrepancy in the case of small  $\alpha$  is smaller is perhaps related to the magnitude of the convective energy flux. The convective energy flux transports energy along surfaces of constant  $r \sin^2(\theta)$  (Quataert & Gruzinov 2000). The magnitude of this flux is proportional to the convective diffusion coefficient  $\alpha_c$ , and a smaller  $\alpha$  corresponds to a smaller  $\alpha_c$  (Narayan et al. 2000). Therefore, when  $\alpha$  is larger, the fluids at the surface are

more strongly heated by the stronger convective energy flux. At last, the bottom right panel shows that the angular momenta of inflow and outflow are almost identical. This is similar to the case of hydrodynamical hot accretion flows (Yuan et al. 2012).

### 3.5. Convective Stability

In the case of hydrodynamical hot accretion flow, it is shown that the inward decrease of inflow rate is because of mass loss in outflow produced by the buoyancy asso-

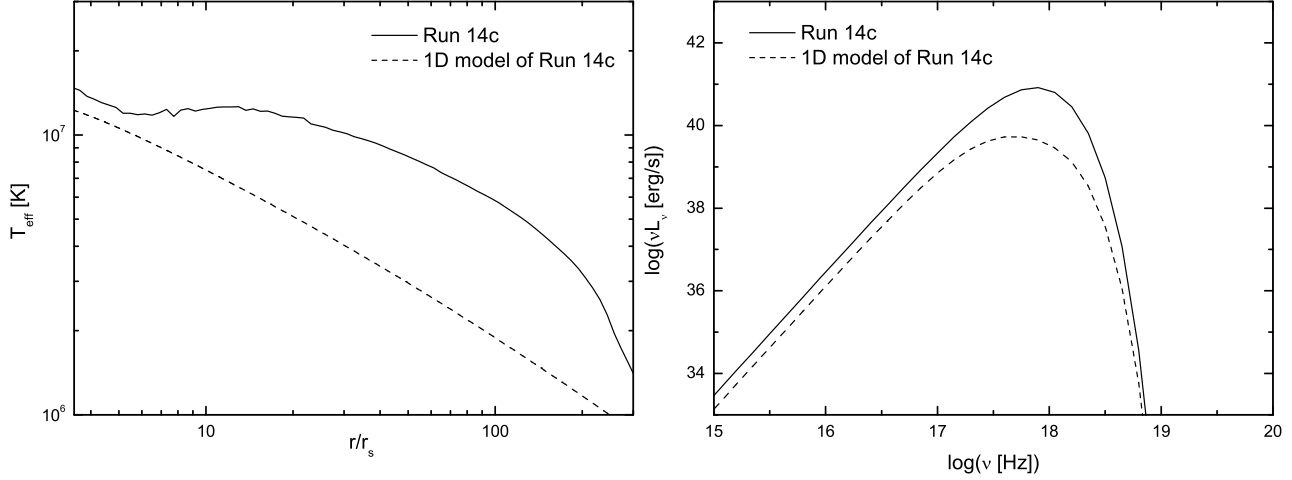


FIG. 13.— Effective temperature (left) and multi-color blackbody spectra (right) of a slim-disk model (Run 5b with  $\alpha = 0.005$  and  $T_{r\phi}$  and  $T_{\theta\phi}$ ). The solid and dashed lines correspond to the numerical simulation and the one-dimensional global solution, respectively.

ciated with convective instability (Yuan et al. 2012). In this section, we analyze the convective stability of the slim disk on the basis of our simulation data.

The energy equation of accretion flows can be written as

$$Q_{\text{adv}}^- = Q_{\text{vis}}^+ - Q_{\text{rad}}^-, \quad (8)$$

where  $Q_{\text{adv}}^- = \Sigma v_r T (dS/dr)$  ( $\Sigma$  is surface density, and  $S$  is the specific entropy). In general,  $Q_{\text{vis}}^+ > Q_{\text{rad}}^-$ , so that  $\Sigma v_r T (dS/dr) > 0$  and  $dS/dr < 0$ . The inward increase of entropy is thought of as a necessary condition of convective instability for rotating flow. A series of simulation studies (Igumenshchev & Abramowicz 1999; Stone et al. 1999; Igumenshchev & Abramowicz 2000; Yuan & Bu 2010) verified that hot accretion flows are convectively unstable, confirming the prediction of Narayan & Yi (1994). Compared with hot accretion flows, the physics of a slim disk is different. In a slim disk, the gas particles can efficiently radiate, but the photons are trapped and hence cannot efficiently escape from the system because of the large scattering optical depth. In addition, a slim disk is supported by the radiation pressure, and hence the specific entropy is dominated by the radiation photons. Sadowski et al. (2009, 2011) found that a radiation pressure-supported disk is convectively unstable. Gu (2012) revisited this problem, taking into account the local energy balance between the viscous heating and the advective and radiative cooling, and found that a slim disk is convectively stable. Gu (2012) thought that the significant difference in the results between their work and Sadowski et al (2009). is probably related to the different approaches for describing the vertical structure. But in Gu (2012), a self-similar solution of the radius is adopted, the consequence of which is unknown.

Here we analyze the convective stability of a slim disk on the basis of our simulation data. We assume that the Höiland criterion (e.g., Begelman & Meier 1982) is applicable to the slim disk. The condition in cylindrical coordinates  $(R, \phi, z)$  for convective stability in a rotating accretion flow (Tassoul 1978) is

$$N_{\text{eff}}^2 = N_R^2 + N_z^2 + \kappa^2 > 0, \quad (9)$$

where  $N_{\text{eff}}$  is defined as an effective frequency,  $\kappa$  is the

epicyclic frequency which is calculated by  $\kappa^2 = \frac{1}{R^3} \frac{\partial l^2}{\partial R}$  ( $l$  is the specific angular momentum), and  $N_R$  and  $N_z$  is the  $R$  and  $z$  component of the well-known Brunt–Väisälä frequency, respectively, which can be calculated by

$$N_R^2 = -\frac{1}{\gamma_r \rho} \frac{\partial P}{\partial R} \frac{\partial S}{\partial R} \quad (10)$$

and

$$N_z^2 = -\frac{1}{\gamma_r \rho} \frac{\partial P}{\partial z} \frac{\partial S}{\partial z}, \quad (11)$$

where  $dS \propto d\ln(\frac{P}{\rho^{\gamma_r}})$ ,  $P$  is the total pressure, and  $\gamma_r$  is the adiabatic index. Here  $P = p_g$  and  $\gamma_r = 5/3$  are employed for the flows of low-density ( $\rho < 10^{-5} \text{ g/cm}^3$ ) and high-gas temperature ( $T_{\text{gas}} > 10^9 \text{ K}$ ) (i.e., outflow or corona region), while  $P = E_0/3$  and  $\gamma_r = 4/3$  are employed for other radiation-dominated flows (i.e., the disk body) where radiation and gas are effectively coupled because of the large scattering opacity.

The results are shown in Figure 12. The left panel is for Run 2b at  $t = 69.233$  orbits, while the right panel for Run 5b at  $t = 230.777$  orbits. The dark region denotes the unstable region, i.e.,  $N_{\text{eff}}^2 < 0$ . We can see that the results are somewhat subtle. For Run 2b nearly half of the region is convectively unstable, while for Run 5b the fraction of the unstable region is much less. Given this result, we can perhaps say that Run 2b is marginally convectively unstable and Run 5b is stable. In both cases, compared with the case of a hydrodynamical hot accretion flow (refer to Figure 6 in Yuan & Bu 2010), the unstable region becomes significantly smaller. We speculate that the difference between the present work and a hydrodynamical hot accretion flow (i.e., Figure 6 in Yuan & Bu 2010) is due to radiation. Recall that in an magnetohydrodynamical hot accretion flow, the magnetic field plays a role of stabilizing the convection (Balbus & Hawley 2002; Narayan et al. 2002). Here radiation plays an effectively similar role although the underlying physics may be different. Physically, when radiation is important as in a slim disk, radiation can directly transport energy, thus the “need” for convection to transport energy becomes weaker. Why is the unstable region in Run 2b larger than that in Run 5b? The only difference



between Run 2b and Run 5b is the value of  $\alpha$ , which is 0.1 and 0.005, respectively. Compared with the case of a large  $\alpha$ , when  $\alpha$  is smaller, the convective energy flux is smaller, thus the role of radiation to stabilize the flow becomes relatively more effective. This explains the difference between Run 2b and Run 5b. This may also explain why the temperature discrepancy between inflow and outflow in Run 2b is larger than in Run 5b (refer to Figure 11).

### 3.6. Multi-color Blackbody Spectra

As an initial step of the application of our numerical simulation, in this section we compare the emitting spectra from two-dimensional numerical simulations and one-dimensional analytical global solutions. For simplicity, we assume a multi-color blackbody spectrum on the basis of effective temperatures. In reality, however, Compton scattering plays an important role in the emitted spectrum (Kawashima et al. 2012). We identify the radiation temperature  $T_{\text{rad}}$  at the photosphere (where the effective optical depth equals 1) as the effective temperature. The effective optical depth is calculated by  $\tau_{\text{eff}} = \sqrt{\tau_{\text{ab}}(\tau_{\text{ab}} + \tau_{\text{sc}})}$ , where  $\tau_{\text{ab}}$  and  $\tau_{\text{sc}}$  are the absorption and Thomson scattering optical depth integrated from the outer boundary along the  $Z$ -direction. We adopt the free free absorption opacity ( $\kappa_{\text{ff}}$ ).

Taking Run 5b as an example, we have calculated the emitted spectrum based on the simulation data. Only the range of  $3.5r_s < r < 80r_s$  is considered. The reason is that only the region of  $r < 80r_s$  has achieved steady state while the region of  $r < 3.5r_s$  is effectively optically thin due to small absorption optical depth caused by high gas temperatures. We also calculate the global solutions of one-dimensional model corresponding to the parameters of Run 5b (refer to Abramowicz et al. 1988 and Watarai et al. 2000 for the calculation approach) and the corresponding spectrum. Figure 13 shows the calculation results. We note that the calculated luminosity based on our two-dimensional numerical simulation agrees well with that obtained by Kawashima et al. (2012). Significant differences of temperature and subsequently emitted spectrum between the two models can be found. This result can give us some initial idea of the difference between simple one-dimensional calculation and the more realistic two-dimensional simulation, which should be useful when applying the slim disk theory to observations. The detailed calculation of the spectrum can be found in Kawashima et al. (2012) and beyond the scope of the present work.

## 4. SUMMARY AND DISCUSSIONS

In this paper, we have performed a two-dimensional radiative hydrodynamical numerical simulation of slim disks. The technical differences between the present work and Ohsuga et al. (2005) are that we include an additional component of viscous stress, i.e.,  $T_{\theta\phi}$ , and consider various values of the viscous parameter  $\alpha$ . We find that the component  $T_{\theta\phi}$  plays an important role in transporting the angular momentum between different latitudes. As a result, compared with the case of no  $T_{\theta\phi}$  component (Ohsuga et al. 2005), the high-latitude outflow (within  $30^\circ$  from the axis) rotates slower, while the flow close to the equatorial plane rotates faster. In addition, we find that the high-latitude outflow has higher density, lower

speed, and a smaller Bernoulli parameter. For the effect of the magnitude of  $\alpha$ , we find that the models with different  $\alpha$  have similar radial structure but different angular structure. The value of  $\alpha$  strongly affects the radial velocity and the value of  $Be$  of outflow at a high latitude.

We have paid more attention in the present work to studying the physics of slim disks. We have calculated the radial profiles of inflow and outflow rates defined by Equations (4) and (5). We have found that both of them decrease inward. Specifically, the inflow rate can be well described by a power law form,  $\dot{M}_{\text{in}} \propto r^s$ . The value of  $s$  is not sensitive to the accretion rate but is mainly dependent on the value of  $\alpha$ . For  $\alpha = 0.1, 0.05, 0.01$ , and  $0.005$ ,  $s \sim 0.37, 0.44, 0.76$ , and  $0.98$ , respectively (Figure 9). Correspondingly, the radial profile of density becomes flatter compared with the case of a constant  $\dot{M}(r)$ . The density profile can be described by  $\rho(r) \propto r^{-p}$ . It is interesting to note that the value of  $p$  is within a narrow range,  $p \approx 0.55$  for  $\alpha \sim 0.005 - 0.1$  (Figure 7).

These results are very similar to a hydrodynamical hot accretion flow. In that case, Yuan et al. (2012) show that the inward decrease of inflow rate is because of the mass loss in outflow. We believe this is also the case for the present slim disk. In the case of hot accretion flows, the mechanism of producing outflow is identified to be buoyancy associated with the convective instability of the accretion flow. To investigate the origin of outflow in the slim disk, we first calculate and compare the properties of inflow and outflow. We have found that the temperature of inflow is lower than that of outflow. The discrepancy is larger when  $\alpha$  is larger (Figure 11). This suggests the existence of convective instability at some level, especially when  $\alpha$  is large. We then analyze the convective stability of the accretion flow on the basis of our simulation data. The result is somewhat subtle. When  $\alpha = 0.1$ , about half of the region of the accretion flow is convectively unstable, but when  $\alpha = 0.005$ , less than half of the region is unstable (Figure 12). Recall that a non-radiative accretion flow is convectively unstable, and we speculate that radiation can stabilize the convection. Physically this is because radiation can also take away energy, like convection. The effectiveness of this stabilizing seems to depend on the magnitude of  $\alpha$ . When  $\alpha$  is smaller, it is more effective, i.e., the accretion flow tends to be more convectively stable (Section 3.5).

Returning to the issue of the radial profile of inflow rate, two questions arise. The first question is what is the mechanism of producing outflow, especially if the slim disk is roughly convectively stable when  $\alpha$  is small? We speculate that the outflow may be produced by radiation force. Or more precisely speaking, both convection and radiation force can produce outflow. Their relative importance may depend on  $\alpha$ . When  $\alpha$  is small, the convective energy flux is weaker, thus radiation force will be the dominant mechanism of producing outflow. The force analysis presented in Figure 5 already suggests the importance of radiation force. We will study this problem in more detail in a future work. If this speculation is correct, the mechanism of producing outflow in slim disks and hot accretion flows is quite different. We note in this context that the angular distribution of the outflow and inflow rates in our simulation are quite different from the case of hot accretion flows (refer to Section 3.4).

This may be evidence for the different origin of outflow in slim disk and hot accretion flows.

Combing the cases of slim disks and the hydrodynamical hot accretion flow, we find that the slope of the radial profile of inflow rate is quite similar, although the mechanisms of producing outflow in the two cases are likely different, as we state above. In fact, the slope is even similar to the case of magnetohydrodynamical hot accretion flow as well. In that case, the mechanism of producing outflow is identified to be a Lorentz force such as magnetocentrifugal force (Yuan et al. 2012; F. Yuan et al. 2013, in preparation). What is the reason for the same slope in spite of different mechanisms? Begelman (2012) may provide an answer to the question of why the hydrodynamical and magnetohydrodynamical hot accretion flows have the same radial profile of inflow rate, see also the summary presented in Yuan et al. (2012). Now the similarity among the three cases seems to indicate that the analysis in Begelman (2012) also applies to radiation-dominated slim disks.

Finally, our whole investigation presented in this paper is based on the assumption that the mass accretion rate can be super-Eddington. However, observations of a large sample of AGNs with 407 sources show that almost all active galactic nuclei (AGNs) are radiating below  $L_{\text{Edd}}$  (Kollmeier et al. 2006). Later, Steinhardt &

Elvis (2010) extended this study to a much larger sample consisting of 62,185 quasars from the Sloan Digital Sky Survey, and they got a similar conclusion (but see Kelly & Shen (2013) for a different opinion). Liu et al. 2013 most recently address this sub-Eddington puzzle. The basic idea is that because of radiative feedback, the mass accretion rate at the inner accretion flow can be self-regulated and thus cannot be super-Eddington. Unfortunately they find that this mechanism cannot fully solve this problem.

We thank Wei-Min Gu and Aleksander Sadowski for helpful discussions and the anonymous referee for constructive comments. This work was supported in part by the Natural Science Foundation of China (grants 11103059, 11121062, 11133005, and 11003052), the National Basic Research Program of China (973 Program 2009CB824800), the CAS/SAFEA International Partnership Program for Creative Research Teams, and the Fundamental Research Funds for the Central Universities (No.CQDXWL-2012-019). The simulations were carried out both at Shanghai Supercomputer Center and the Super Computing Platform of Shanghai Astronomical Observatory.

#### REFERENCES

- Abramowicz, M. A., Czerny, B., Lasota, J. P., & Szuszkiewicz, E. 1988, *ApJ*, 332, 646
- Balbus, S. A., & Hawley, J. F. 1998, *RvMP*, 70, 1
- Balbus, S. A., & Hawley, J. F. 2002, *ApJ*, 573, 749
- begelman2012 Begelman, M. C. 2012, *ApJ*, 749, 3
- Begelman, M. C., & Meier, D. L. 1982, *ApJ*, 253, 873
- Blandford, R. D., & Begelman, M. 1999, *MNRAS*, 303, 1
- Blandford, R. D., & Begelman, M. 2004, *MNRAS*, 349, 68
- Bu, D., Yuan, F., Wu, M., & Cuadra J. 2013, *MURAS*, 434, 1692
- Eggum, G. E., Coroniti, F. V., & Katz, J. I. 1987, *ApJ*, 323, 634
- Eggum, G. E., Coroniti, F. V., & Katz, J. I. 1988, *ApJ*, 330, 142
- Gu, W. M. 2012, *ApJ*, 753, 118
- Hawley, J. F., Gammie, C. F., & Balbus, S. A. 1995, *MNRAS*, 272, 828
- Hawley, J. F., Gammie, C. F., & Balbus, S. A. 1996, *ApJ*, 464, 690
- Hirose, S., Krolik, J. H., & Blaes, O., 2009, *ApJ*, 691, 16
- Igumenshchev, I. V., & Abramowicz, M. A. 1999, *MNRAS*, 303, 309
- Igumenshchev, I. V., & Abramowicz, M. A. 2000, *ApJS*, 130, 463
- Jiang, Y. F., Stone, J. M., & Davis, S. W., 2013, *ApJ*, 778, 65
- Kato, S., Fukue, J., & Mineshige, S. 1998, *Black-Hole Accretion Disks* (Kyoto, Japan: Kyoto Univ. Press)
- Kelly, B., & Shen, Y. 2013, *ApJ*, 764, 45
- Kollmeier, J. A., Onken, C. A., Kochanek, C. S., et al. 2006, *ApJ*, 648, 128
- Kawashima, T., Ohsuga, K., Mineshige, S., et al. 2012, *ApJ*, 752, 18
- Levermore, C. D., & Pomraning, G. C. 1981, *ApJ*, 248, 321
- Li, J., Ostriker, J., & Sunyaev, R. 2013, *ApJ*, 767, 105
- Liu, C., Yuan, F., Ostriker, J. P., Gan, Z., & Yang, X. H. 2013, *MNRAS* 434, 1721
- Mineshige, S., Kawaguchi, T., & Takeuchi, M. 2000, *NewAR*, 44, 435
- Narayan, R., Igumenshchev, I. V., & Abramowicz, M. A. 2000, *ApJ*, 539, 798
- Narayan, R., Quataert, E., Igumenshchev, I. V., & Abramowicz, M. A., 2002, *ApJ*, 577, 295
- Narayan, R., Sadowaki, A., Penna, R., & Kulkarni, A. K. 2012, *MNRAS*, 426, 3241
- Narayan, R., & Yi, I. 1994, *ApJ*, 428, 13
- Ohsuga, K., & Mineshige, S. 2007, *ApJ*, 670, 1283
- Ohsuga, K., & Mineshige, S., Mori, M., Umemura, M. 2002, *ApJ*, 574, 315
- Ohsuga, K., Mineshige, S., & Watarai, K. 2003, *ApJ*, 596, 429
- Ohsuga, K., Mori, M., Nakamoto, T., & Mineshige, S. 2005, *ApJ*, 628, 368
- Okuda, T. 2002, *PASJ*, 52, 253
- Okuda, T., Teresi, V., Toscano, E., & Molteni, D. 2005, *MNRAS*, 357, 295
- Paczynski, B., & Wiita, P. J. 1980, *A&A*, 88, 23
- Pringle, J. E. 1981, *ARA&A*, 19, 137
- Quataert, E., & Gruzinov, A. 2000, *ApJ*, 539, 809
- Sadowski, A., Abramowicz, M., Bursa, M., et al. 2009, *A&A*, 502, 7
- Sadowski, A., Abramowicz, M., Bursa, M., et al. 2011, *A&A*, 527, A17
- Sadowski, A., Narayan, R., Penna, R., & Zhu, Y. 2013, *arXiv:1307.1143*
- Shakura, N. I., & Sunyaev, R. A. 1973, *A&A*, 24, 337
- Steinhardt, C. L., & Elvis, M. 2010, *MNRAS*, 402, 263
- Stone, J. M., Hawley, J. F., Gammie, C. F., & Balbus, S. A. 1990, *ApJ*, 463, 656
- Stone, J. M., & Pringle, J. E. 2001, *MNRAS*, 322, 461
- Stone, J. M., Pringle, J. E., & Begelman, M. C. 1999, *ApJ*, 310, 1002
- Tassoul, J. L., 1978, *Theory of Rotating Stars* (Princeton, NJ: Princeton Univ. Press)
- Vierdayanti, K., Mineshige, S., Ebisawa, K., & Kawaguchi, T. 2006, *PASJ*, 58, 915
- Wang, J. M., & Zhou, Y. Y. 1999, *ApJ*, 516, 420
- Watarai, K., Fukue, J., Takeuchi, M., & Mineshige, S. 2000, *PASJ*, 52, 133
- Watarai, K., Mizuno, T., & Mineshige, S. 2001, *ApJL*, 549, L77
- Yuan, F. 2001, *MNRAS*, 324, 119
- Yuan, F., & Bu, D. 2010, *MNRAS*, 408, 1051
- Yuan, F., Bu, D., & Wu, M. 2012, *ApJ*, 761, 130
- Yuan, F., Wu, M., & Bu, D. 2012, *ApJ*, 761, 129

